Resorcinarene cavitand based morphologically distinct polymers as templates for iridium electrocatalysts

Binh Le
Advisor: Dr. Bala Ramjee
Department of Chemistry & Biochemistry, Old Dominion University

Abstract: Proton exchange membrane water electrolysis represents a leading technology for sustainable hydrogen production, but its widespread deployment is constrained by the scarcity and high loading requirements of iridium-based oxygen evolution reaction catalysts. Template-directed synthesis offers a promising route to morphologically controlled precious metal nanostructures that maximize active surface area and reduce precious metal utilization. This work reports the use of photopolymerized resorcinarene tetraalkene tetrathiol (RTATT) fibrous scaffolds in ethyl acetate as templates for the synthesis of palladium monometallic and palladium-iridium bimetallic nanostructures. RTATT fibers were characterized by ^{1}H NMR spectroscopy, confirming partial thiol-ene conversion and retention of both thioether linkages and residual alkene and thiol functionality within the polymer scaffold. Direct reductive synthesis of palladium nanostructures on unfunctionalized and hexene-functionalized RTATT fibers was investigated across two Pd-to-thiol stoichiometries, revealing a strong dependence of nanoparticle distribution and aggregate morphology on the metal-to-thiol ratio. Palladium-iridium bimetallic nanostructures were subsequently accessed through galvanic exchange of the Pd-RTATT fiber composites with iridium(III) chloride. TEM and EDS characterization confirmed substantial galvanic displacement of palladium by iridium, yielding densely packed nanoparticles of 2 to 6 nm distributed along the fiber scaffold. The inclusion of tetrabutylammonium bromide during galvanic exchange produced a markedly different morphology, affording discrete nanoparticles of 15 to 75 nm arranged in chain-like assemblies along the fibrous template. These results establish RTATT fibrous scaffolds as viable templates for compositionally and morphologically tunable bimetallic nanostructures.

Introduction

Proton exchange membrane water electrolysis (PEMWE) has emerged as the leading electrochemical technology for converting water to hydrogen and oxygen PEMWE offers distinct advantages including high current density operation, compact system design, In PEMWE systems, water oxidation proceeds at the anode through the oxygen evolution reaction (OER), while hydrogen evolution occurs concurrently at the cathode. The OER constitutes the thermodynamically and kinetically unfavorable half-reaction and thereby represents the rate-limiting step that governs the overall efficiency of the electrolysis process. Consequently, improvements in OER catalytic activity, current efficiency, and operational stability are critical to enhancing PEMWE system performance and enabling practical deployment of water electrolysis technology.

Iridium-based catalysts represent the current state-of-the-art for oxygen evolution reaction catalysis in PEMWE systems, having achieved unparalleled activity and stability across diverse operational environments.[1] The exceptional performance of iridium catalysts derives from their ideal binding energy for oxygen-containing intermediates, their ability to sustain electrochemical activity across broad temperature and pH ranges, and their remarkable corrosion resistance in the acidic, oxidative conditions inherent to the anode environment of proton exchange membrane electrolyzers.[1] However, the widespread deployment of iridium-based OER catalysts is fundamentally constrained by two interconnected challenges: the extreme scarcity of iridium as a naturally occurring element and its correspondingly high market cost. Annual global iridium production reaches only approximately seven to nine tons rendering it among the rarest elements on Earth and creating severe supply limitations for large-scale electrolyzer manufacturing.[2] Furthermore, conventional iridium-based OER catalysts require substantial precious metal loadings at the anode, typically ranging from 2.0 to 3.0 milligrams of iridium per square centimeter of electrode surface, which significantly elevates the capital cost of water electrolysis systems and undermines their economic viability for widespread adoption.[3] The United States Department of Energy has established ambitious technical targets to address this constraint, specifying a reduction in total platinum group metal content in PEM electrolyzers from current levels of 3.0 milligrams per square centimeter to 0.5 milligrams per square centimeter by 2026, with an ultimate target of 0.125 milligrams per square centimeter by 2030, while simultaneously maintaining performance standards and durability requirements.[4] These aggressive reduction targets necessitate fundamental advances in iridium nanostructure design and catalyst morphology optimization that maximize atomic efficiency and exploit the electrochemically active surface area without compromising the inherent catalytic performance and stability characteristics that distinguish iridium among precious metal catalysts.

In response to these stringent precious metal loading constraints and the fundamental necessity for enhanced catalyst efficiency, two complementary

strategies have emerged from recent literature to simultaneously improve iridium catalyst activity while substantially reducing the required precious metal content: the incorporation of secondary metals through compositional alloying and the deliberate engineering of nanostructure morphology to maximize surface utilization.[5] The introduction of foreign metals into iridium-based catalysts via alloying has been shown to modify both the electronic and geometric properties of the active sites, thereby tuning the binding energy of oxygen-containing reaction intermediates and improving overall oxygen evolution kinetics. The alloying approach functions through a synergistic mechanism in which secondary metals induce a shift in the d-band center of iridium, thereby optimizing the adsorption and desorption kinetics of reaction intermediates while simultaneously reducing the total mass of precious metal required per unit catalytic performance.[6]

Concurrent with advances in compositional control through alloying, the morphological engineering of iridium nanostructures has emerged as an equally powerful approach to maximize electrochemically active surface area and thereby enhance the intrinsic utilization of precious metal atoms.[5] One-dimensional nanostructures such as nanowires and nanodendrites offer substantial advantages due to their high aspect ratios, large exposed surface areas, and preferential exposure of active crystallographic facets.[7] Two-dimensional morphologies including nanosheets similarly maximize surface exposure while offering unique electronic properties arising from their planar geometry.[7] By synergistically combining compositional control through transition metal alloying with morphological engineering at the nanoscale, researchers have achieved substantial reductions in iridium loading from conventional levels of 2.0 to 3.0 milligrams per square centimeter down to 0.35 milligrams per square centimeter while simultaneously maintaining or enhancing overall catalytic activity and operational stability.[8] These advances demonstrate that precise control of both nanostructure geometry and elemental composition represents a promising and feasible materials chemistry approach to addressing the cost and scarcity constraints that presently limit large-scale deployment of PEMWE technology.

Template-directed synthesis has emerged as a powerful and versatile methodology to direct the growth of inorganic nanostructures into predetermined morphologies with excellent size uniformity and well-defined crystallographic properties.[9] Recent advances in template-directed synthesis have demonstrated transformative catalytic benefits for precious metal nanostructures across multiple systems.[10-12] A notable recent advancement employed a poly(styrene)-block-poly(vinylpyridine)-block-poly(ethylene oxide) triblock copolymer as a structure-directing agent to synthesize dendritic high-entropy alloy nanoparticles incorporating iridium alongside platinum, palladium, silver, and ruthenium, with the block copolymer serving as a confined nucleation template that promoted single-phase formation and uniform metal distribution while enabling facile removal through simple solvent extraction post-synthesis.[13] Furthermore, comprehensive studies on block copolymer template-directed synthesis of ordered metallic nanostructures have established methodologies for fabricating two-dimensional metal nanosheets materials with iridium and other precious metals, demonstrating that the architectural control afforded by block copolymer self-assembly can be effectively extended across an entire class of catalytically significant metals to produce well-defined, replicable nanostructures unattainable through conventional synthetic approaches.[14] These recent demonstrations establish that template-directed approaches provide not just marginal improvements but rather transformative enhancements in catalyst utilization and performance, particularly when soft polymeric templates are employed to enable precise compositional and morphological control of precious metal nanostructures.

Our research group has established a direct, template- and surfactant-free approach to the synthesis of morphologically tunable polymeric nanostructures through the thiol-ene photopolymerization of resorcinarene tetra alkene tetra thiol (RTATT), an amphiphilic cavitand monomer synthesized in four steps from resorcinol and bearing four terminal alkene tails and four upper-rim thiol groups in an intrinsic 1:1 stoichiometric ratio (**Figure 1**).[15]

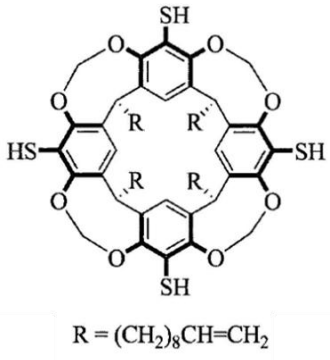

Figure 1: Schematic depiction of resorcinarene tetra alkene tetra thiol (RTATT) structure.

Upon UV irradiation, RTATT undergoes free radical thiol-ene photopolymerization through a step-growth mechanism initiated by homolytic cleavage of the sulfur-hydrogen bond to generate a thiyl radical,

which adds across a pendant alkene group and propagates through sequential chain transfer events. The identity of the photopolymerization solvent exerts decisive control over the morphology of the resulting polymer architecture: irradiation in chloroform yields hollow nanocapsules with an average diameter of approximately 106 nm, irradiation in ethyl acetate produces extended one-dimensional fibrous networks and interconnected fiber assemblies approximately 50 nm in width, and irradiation in tetrahydrofuran and dichloromethane affords polydisperse nanoparticles and distorted honeycomb-like lattice structures, respectively, demonstrating that a broad range of polymeric nanostructure geometries is accessible from a single monomer through systematic variation of reaction solvent alone. Because thiol-ene photopolymerization proceeds to partial rather than complete conversion under the conditions employed, the resulting RTATT polymer retains both sulfide linkages formed through thiol-ene addition and a population of unreacted thiol groups within the same scaffold, regardless of the morphological form obtained.The sulfide linkages and thiol functional groups inherent to the RTATT polymer scaffold provide multivalent binding sites capable of stabilizing metal nanoparticles both inside and outside the polymer shell. Our group showed that RTATT nanocapsules could direct the synthesis of gold nanostructures through a modified Brust-Schiffrin approach (**Figure 2**), with the morphology of the resulting product depending critically on reaction conditions, particularly the metal salt to thiol ratio; specifically, continuous gold nanoshells approximately 12 nm in thickness form at a sulfur-to-gold molar ratio of 0.5, while spherical aggregates of closely packed individual nanoparticles form at a sulfur-to-gold molar ratio of 0.8.[16] The nanocapsule-templated gold nanoparticle aggregates demonstrated catalytic utility in model reduction reactions.

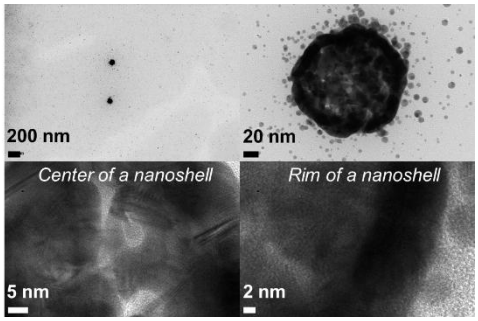

Figure 2: TEM analysis of gold nanostructure templated within photopolymerized resorcinarene-nanocapsule framework.[16]

Beyond the hollow nanocapsular architectures obtained through photopolymerization in chloroform, our research has established that solvent selection exerts critical control over RTATT polymer morphology, enabling the synthesis of fibrous architectures.[15] Photopolymerization of RTATT in ethyl acetate yields extended one-dimensional fibrous morphologies and interconnected fiber networks (**Figure 3**), a transformation arising from differences in reaction kinetics and phase separation behavior characteristic of the ethyl acetate solvent system. These RTATT fibers maintain the ubiquitous sulfide and alkene functional groups present in the nanocapsule variants while offering substantially enhanced accessibility for metal precursor coordination compared to the confined interior environments of hollow nanocapsules.

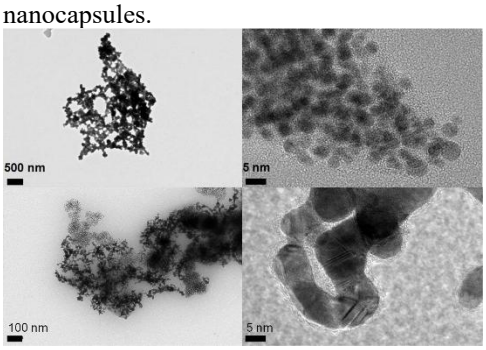

Figure 3: TEM analysis of resorcinarene-fibers framework.

The ability to selectively obtain either nanocapsular or fibrous polymeric templates through systematic variation of photopolymerization solvent, combined with the retention of surface-coordinating functional groups across all morphological variants, establishes a versatile synthetic platform applicable to diverse precious metal systems and target nanostructure geometries. Our group's demonstrated success with gold and platinum nanostructures provides a highly motivational precedent for extending the RTATT templating approach to the synthesis of iridium catalysts for oxygen evolution applications.

This work reports the RTATT fiber-templated synthesis of palladium monometallic and palladium-iridium bimetallic nanostructures as a foundational step toward developing morphologically controlled iridium catalyst architectures for oxygen evolution applications. Photopolymerized RTATT fibers in ethyl acetate are employed as templates for the direct reductive synthesis of palladium nanostructures, with the effects of Pd-to-thiol stoichiometry and fiber surface functionalization on the resulting nanoparticle morphology and distribution examined systematically. Palladium-iridium bimetallic nanostructures are subsequently accessed through galvanic exchange of the Pd-RTATT fiber composites with iridium(III) chloride, and the

influence of tetrabutylammonium bromide as a phase-transfer additive on the exchange product morphology and composition is characterized by transmission electron microscopy and energy-dispersive X-ray spectroscopy.

General remarks

Resorcinol (MP Biomedicals), and 10-undecanal (>95%, Aldrich) were used for the acid-catalyzed condensation step. N-bromosuccinimide (99%, Acros) was recrystallized before use for the bromination step. Bromochloromethane (98%, SynQuest Labs) was used as received for cavitand formation. Cesium carbonate (99%, Alfa Aesar) dried under heat and vacuum. n-Butyllithium (2.5M, Aldrich) and elemental sulfur were used for the final thiolation step. THF and toluene were dried and distilled using sodium metal and benzophenone, ethyl acetate were dried and distilled with calcium hydride.

Sodium tetrachloropalladate (98%, Aldrich) tetraoctylammonium bromide (Aldrich), tetrabutylammonium bromide (>98%, Aldrich), sodium borohydride (99% Thermo Scientific), iridium(III) chloride hydrate (TCI), 1-hexene (97%, Acros), and 200 proof ethanol (Decon Laboratories) employed for palladium monometallic and palladium-iridium nanostructures were used as received. Barnstead Nanopure water (18.2 MΩ cm) was used for all aqueous steps.

Photopolymerizations was carried in a Srinivasan-Griffin Rayonet photochemical reactor. The reactor was equipped with four 254 nm and four 300 nm lamps, supplied by the Southern New England Ultraviolet Company.

Synthesis of resorcinarene tetra-alkene tetra-thiol (RTATT)

RTATT cavitand surfactant was synthesized in four steps according to the methods described in previous work.[15] Resorcinol and 11-undecenal undergo acid-catalyzed condensation to form resorcinarene. Resorcinarene is combined with bromochloromethane and cesium carbonate under sealed-tube conditions to form the corresponding cavitand through acetal bridging of adjacent phenolic hydroxyl groups. The cavitand then undergoes electrophilic bromination with N-bromosuccinimide to install four aryl bromide substituents at the upper rim, yielding bromocavitand. Finally, the bromocavitand is treated with n-butyllithium followed by quenching with elemental sulfur to yield RTATT cavitand surfactant (**Figure 4**).

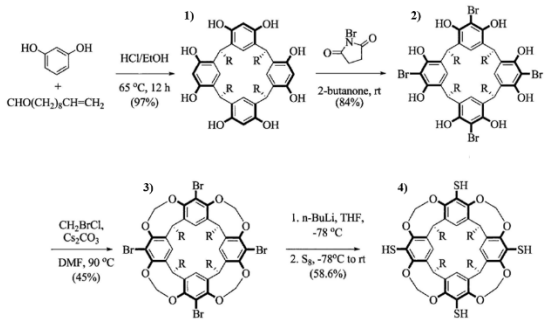

Figure 4: Schematic illustration of resorcinarene tetra-alkene tetra-thiol (RTATT).

Synthesis of RTATT fibers

RTATT was dissolved in distilled ethyl acetate and filtered through a 0.45 micron nylon filter into a quartz tube. The contents were degassed by purging with argon for 30 seconds and sealed. The sealed quartz tube was placed in a Rayonet photoreactor for 15 minutes.

Synthesis of Palladium (Pd) monometallic nanostructures

Na_2PdCl_4 (0.0179 g, 0.0609 mmol Pd) was dissolved in 5 mL nanopure water. Tetraoctylammonium bromide 0.102 g solubilized in 10 mL distilled ethyl acetate was added and the mixture was stirred under argon for 30 minutes. RTATT) was then added and stirred under argon for an additional 30 minutes. To probe to the effect of RTATT concentration on the resulting palladium nanoparticles his procedure was carried out in two variations differing in the volume of 1.5 mM RTATT added: 9 mL (0.054 mmol sulfide, 1.13 equiv Pd per RTATT-sulfide) and 4.5 mL (0.027 mmol sulfide, 2.26 equiv Pd per RTATT-sulfide). The reaction round bottom flask was placed in an ice bath and stirred for 5 minutes. 2mL 0.443 M ice cold $NaBH_4$ in nanopure water was added via syringe in a single injection and the mixture was stirred on ice under argon for 1 hour. The product was washed three times with 10 mL nanopure water.

Synthesis of Palladium-Ir (PdIr) bimetallic nanostructures by galvanic exchange

To a 3 mL aliquot of Pd-RTATT fiber solution in a one-neck round bottom flask, tetrabutylammonium bromide (454 mg, 1.408 mmol) was added. IrCl3 (3 mL of a 9.3 mg / 8.5 mL stock solution in 200 proof ethanol, 0.0110 mmol Ir) was then added to the flask. The mixture was stirred under argon at 90 °C with reflux. The product was purified by two rounds of centrifugation and precipitation with 200 proof ethanol.

This procedure was also carried out in the absence of tetrabutylammonium bromide to evaluate its effect on the resulting nanoparticles.

Functionalization of RTATT fibers with short chain ligand, 2-mercaptoethylamine hydrochloride

To a quartz tube containing RTATT fibers (1.5 mM), 1-hexene (4 equivalence) was added and the mixture degassed by purging with argon for 30 seconds. The mixture was irradiated under the same photopolymerization conditions as the 1.5 mM RTATT fibers for 30 minutes. 2-Mercaptoethylamine hydrochloride (4 equivalence) was then added to the quartz tube, the contents were degassed with argon for 30 seconds then irradiated for an additional 30 minutes under the same conditions. Insoluble precipitants were observed to form during this stage. The product was purified by two rounds of centrifugation and precipitation with 200 proof ethanol.

Functionalization of RTATT fibers with long chain ligand, 11-mercaptoundecyl-N,N,N-trimethylammonium bromide

RTATT fibers (1.5 mM) was combined with 11-mercaptoundecyl-N,N,N-trimethylammonium bromide (2 equivalence) in quartz tube and degassed by purging with argon for 30 seconds. The mixture was irradiated under the same photopolymerization conditions as the 1.5 mM RTATT fibers for 30 minutes. 1-hexene (4 equivalence) was then added to the quartz tube, the contents were degassed with argon for 30 seconds then irradiated for an additional 30 minutes under the same conditions. Insoluble precipitants were observed to form during this stage. The product was purified by one round of centrifugation and precipitation with 200 proof ethanol.

Synthesis of Palladium (Pd) monometallic nanostructures with hexene functionalized fibers

Na_2PdCl_4 (0.0551 mmol Pd) was stirred with tetrabutylammonium bromide (0.2755 mmol) solubilized in distilled ethyl acetate for 30 minutes under argon at room temperature. The resulting organic phase was transferred into a round bottom flask following phase separation. 8 mL of RTATT polymer fibers (1.5 mM) functionalized with 4 equivalents of hexene were added to the flask and stirred under argon for 30 minutes. The reaction flask was then placed in an ice bath and stirred for 5 minutes. 0.442 M of ice cold $NaBH_4$ in nanopure water was added via syringe in a single injection and the mixture was stirred on ice under argon for 1 hour. The product was washed three times with 10 mL nanopure water.

Results and Discussions

Synthesis of RTATT monomers was successfully carried out and compared with the photopolymerized RTATT fibers post-photopolymerization. Comparison of the ^{1}H NMR spectra of the RTATT monomer and the photopolymerized product in CDCl3 reveals attenuation of the terminal alkene signals at approximately 4.9 and 5.7 ppm in the photopolymer relative to the monomer, with residual low-intensity signals persisting in this region. Similarly, the thiol region at approximately 2.5 to 3.0 ppm shows broadened and shifted intensity in the photopolymer compared to the monomer. Both observations are consistent with partial consumption of the alkene and thiol functional groups during photopolymerization, with unreacted alkene and thiol groups retained within the polymer scaffold.

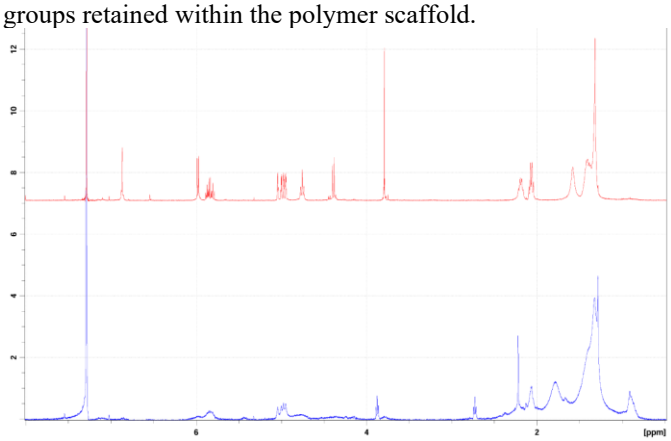

Figure 5: NMR spectra comparison of RTATT monomers (top, red) and RTATT photopolymers.

Preliminary photopolymerization of RTATT monomers at varying concentrations yielded fibers that produced similar results from previous work when examining by TEM and HRTEM analysis (**Figure 5**). RTATT fibers were successfully obtained and exhibited fractal-like interconnected cluster morphologies consistent with previously reported work. The network cluster features observed in panel a span approximately 50 to 350 nm in their widest dimension, while those in panel b are distributed across a comparable range of approximately 30 to 200 nm. Overall, varying concentrations of RTATT monomer before photopolymerization shows a slight to near negligible morphological change in the earlier stage of investigation.

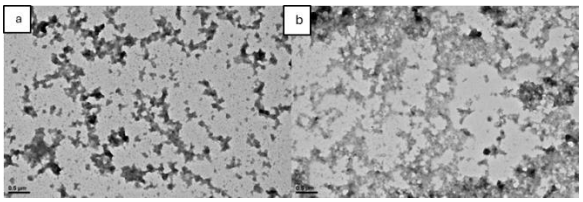

Figure 6: TEM analysis of photopolymerized RTATT at varying concentrations, **a)** 0.5 mM **b)** 3.0 mM.

Unfunctionalized RTATT fibers was employed for the direct synthesis of monometallic Pd onto the polymer. At a Pd-to-thiol ratio of 1.13:1, TEM analysis revealed the formation of irregularly shaped, amorphous aggregates in which Pd nanoparticles appear as discrete dark domains distributed nonuniformly throughout the fibrous polymer template (**Figure 7**). The aggregates span equivalent diameters of approximately 100 to 750 nm, with the majority ranging from 100 to 550 nm, and exhibit a morphology appearing to be uncontrolled particle clustering rather than templated growth. The Pd nanoparticles appear concentrated at regions of higher polymer density while remaining sparse or absent in surrounding areas, suggesting that at this elevated metal-to-thiol ratio the available thiol binding sites are insufficient to uniformly coordinate and spatially confine the metal precursor prior to reduction, resulting in localized nucleation and aggregation rather than a dispersed nanoparticle distribution throughout the fiber network. At higher magnification, Pd nanoparticles can be seen nucleating preferentially along the fibrous polymer template in a distinctive chain-like arrangement which suggests growth directing influence from the fiber polymer template.

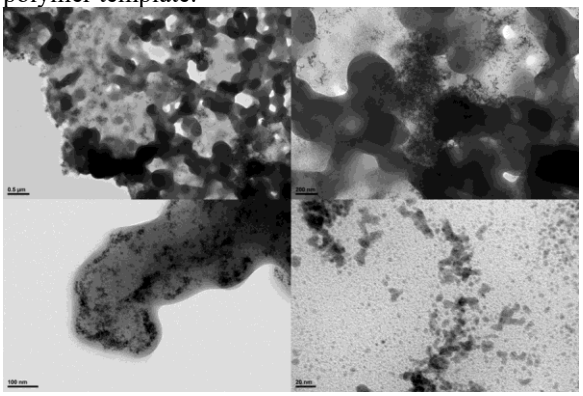

Figure 7: TEM analysis of Pd nanostructures synthesized within RTATT fiber template at a Pd-to-sulfide ratio of 1.13:1, showing nonuniform clustering of Pd nanoparticles localized mostly along the outer rim of the fiber.

When a Pd-to-thiol ratio of 1.13:1 was employed, TEM analysis revealed a markedly different morphology characterized by a substantially higher density of Pd nanoparticles distributed more uniformly throughout the fibrous polymer template (**Figure 8**). The particles forms a dense colony of discrete particles, continuously coating along the fiber network rather than isolated aggregated clusters. This more uniform dispersion is consistent with a greater availability of thiol coordination sites per metal center at the lower Pd-to-thiol ratio, which facilitates spatial confinement and stabilization of individual metal nuclei prior to and during reduction, suppressing the uncontrolled aggregation observed under metal-excess conditions.

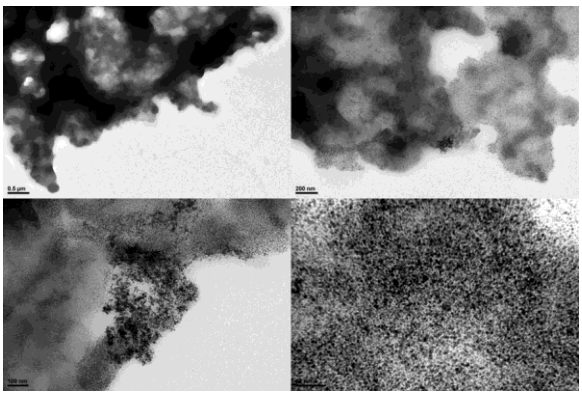

Figure 8: TEM analysis of Pd nanostructures synthesized at a Pd-to-sulfide ratio of 2.26:1, showing chain-like alignment of Pd nanoparticles nucleated along the RTATT fibrous polymer template.

Furthermore, RTATT photopolymer fibrous networks functionalized with 4 equivalents of 1-hexene were employed as templates for the direct reduction synthesis of Pd nanostructures to investigate the effect of thiol-ene surface functionalization on nanoparticle morphology and particle distribution within the fiber scaffold. TEM analysis of Pd nanoparticles synthesized on hexene-functionalized fibers at an equivalent 2.26:1 Pd-to-thiol ratio reveals a notably different morphology compared to the unfunctionalized fiber system (**Figure 9**). Rather than the chain-like particle alignment observed along discrete fiber strands, the hexene-functionalized sample displays a more continuous and uniform distribution of Pd nanoparticles throughout a denser, interconnected polymer network. This distinction suggests that thiol-ene functionalization of the fiber surface with 1-hexene alters the spatial distribution of metal-coordinating sites, promoting a more even and uniform coating of Pd nanoparticles across the entire fiber network surface, rather than localized growth along the length of individual fibers.

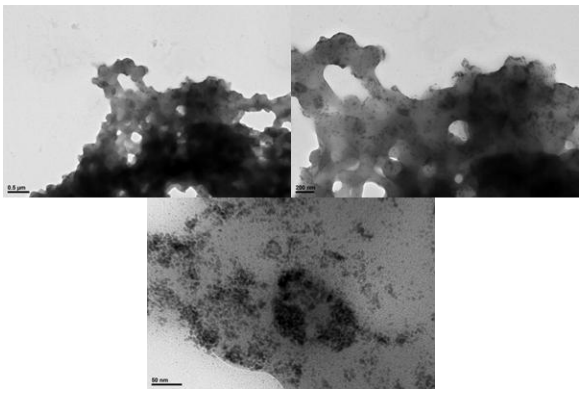

Figure 9: TEM analysis of Pd nanostructures synthesized at a 1.15:1 Pd-to-thiol ratio of, showing chain-like alignment of Pd nanoparticles nucleated distributed sparsely within the polymeric fiber network.

Fabricated Pd nanostructures were further reacted with iridium (III) chloride hydrate via galvanic exchange, and the resulting PdIr bimetallic nanostructures were characterized by TEM and EDS. When the galvanic exchange reaction was carried out in the absence of the bromide source tetrabutylammonium bromide, TEM analysis of the PdIr product confirmed retention of the RTATT fibrous morphology, with a densely packed, nearly continuous coating of nanoparticles distributed uniformly along the fiber scaffold (**Figure 10**). Particle size analysis from the TEM indicates a mean diameter of approximately 3-4 nm, with the majority of particles falling in the 2-6 nm range and only occasional larger particles approaching 7-8 nm, reflecting a relatively narrow and unimodal size distribution. EDS analysis established an Ir:Pd atomic ratio of 0.9:0.7, confirming substantial galvanic displacement of Pd by Ir to afford the bimetallic nanostructure.

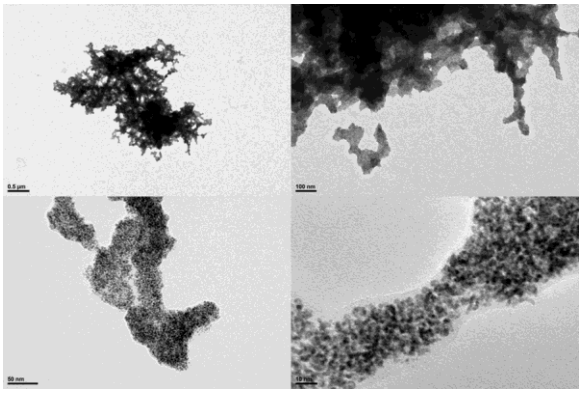

Figure 10: TEM analysis of PdIr bimetallic nanostructures synthesized via galvanic exchange of RTATT fiber-templated Pd nanostructures with $IrCl_3$. Panels display increasing magnification.

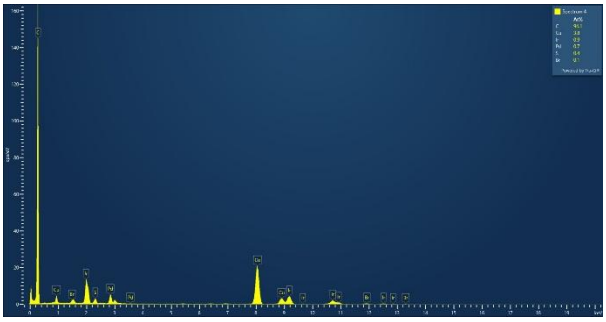

Figure 11: EDS analysis of PdIr bimetallic structure synthesized without the presence of tetrabutylammonium bromide.

TEM analysis of the TBABr-mediated galvanic exchange product revealed a markedly different morphology, with discrete nanoparticles of substantially increased size arranged in chain-like assemblies along the RTATT fibrous scaffold (**Figure 12**). In contrast to the continuous, densely packed nanoparticle coating observed under TBABr-free conditions. Size analysis indicates a particle diameter distribution spanning approximately 15-75 nm, with a median of approximately 35-40 nm and a mean of approximately 40-45 nm, reflecting a broader and more polydisperse population than that observed in the absence of TBABr. The marked increase in particle size and the shift from a continuous fibrous coating to localized, spatially separated nanoparticles suggests that bromide coordination to surface Pd sites under TBABr-mediated conditions suppressed nucleation events and promoted growth on fewer, larger crystallites rather than uniform deposition across the fiber network.

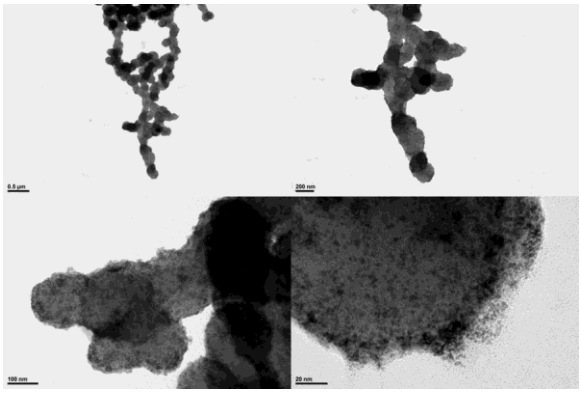

Figure 12: TEM analysis of PdIr bimetallic nanostructures synthesized via galvanic exchange of RTATT fiber-templated Pd nanostructures with $IrCl_3$ in the presence of tetrabutylammonium bromide.

Conclusion

Resorcinarene tetraalkene tetrathiol fibrous scaffolds photopolymerized in ethyl acetate were demonstrated as viable templates for the synthesis of

palladium monometallic and palladium-iridium bimetallic nanostructures. The Pd-to-thiol stoichiometry was found to govern nanoparticle distribution and aggregate morphology within the fiber network, with higher thiol availability promoting more uniform nanoparticle dispersion along the scaffold. Galvanic exchange of Pd-RTATT fiber composites with iridium(III) chloride afforded PdIr bimetallic nanostructures with confirmed iridium incorporation by EDS, yielding densely packed 2 to 6 nm nanoparticles along the fiber scaffold under bromide-free conditions. The inclusion of tetrabutylammonium bromide during galvanic exchange produced a distinct morphological outcome, affording discrete 15 to 75 nm nanoparticles arranged in chain-like assemblies, demonstrating that bromide coordination serves as an accessible handle for nanoparticle size and spatial distribution control within the RTATT templating platform. Collectively, these results establish RTATT fibrous scaffolds as a versatile and chemically tunable template for bimetallic precious metal nanostructure synthesis and support the broader application of this platform toward the development of morphologically controlled iridium-based catalysts for oxygen evolution in proton exchange membrane water electrolysis.

References

(1) Galyamin, D.; Tolosana-Moranchel, Á.; Retuerto, M.; Rojas, S. Unraveling the Most Relevant Features for the Design of Iridium Mixed Oxides with High Activity and Durability for the Oxygen Evolution Reaction in Acidic Media. *JACS Au* **2023**, *3* (9), 2336-2355. DOI: 10.1021/jacsau.3c00247.

(2) Smith, B., Graziano, D., Riddle, M., Liu, D.-J., Sun, P., Iloeje, C., Kao, E., & Diamond, D. (2022). Platinum Group Metal Catalysts: Supply Chain Deep Dive Assessment. https://doi.org/10.2172/1871583

(3) Knöppel, J.; Möckl, M.; Escalera-López, D.; Stojanovski, K.; Bierling, M.; Böhm, T.; Thiele, S.; Rzepka, M.; Cherevko, S. On the limitations in assessing stability of oxygen evolution catalysts using aqueous model electrochemical cells. *Nature Communications* **2021**, *12* (1), 2231. DOI: 10.1038/s41467-021-22296-9.

(4) https://www.energy.gov/eere/fuelcells/technical-targets-proton-exchange-membrane-electrolysis

(5) Wang, H.; Li, X.; Zhang, G.; Gu, Z.; Chen, H.; Wei, G.; Shen, S.; Cheng, J.; Zhang, J. Recent Progress in Balancing the Activity, Durability, and Low Ir Content for Ir-Based Oxygen Evolution Reaction Electrocatalysts in Acidic Media. *Small* **2025**, *21* (6), 2410407. DOI: https://doi.org/10.1002/smll.202410407 (acccessed 2026/04/03).

(6) Wu, Q.; Gao, Q.; Wang, X.; Qi, Y.; Shen, L.; Tai, X.; Yang, F.; He, X.; Wang, Y.; Yao, Y.; et al. Boosting electrocatalytic performance via electronic structure regulation for acidic oxygen evolution. *iScience* **2024**, *27* (1), 108738. DOI: 10.1016/j.isci.2023.108738 From NLM.

(7) Wang, C.; Feng, L. Recent advances and perspectives of Ir-based anode catalysts in PEM water electrolysis. *Energy Advances* **2024**, *3* (1), 14-29, 10.1039/D3YA00492A. DOI: 10.1039/D3YA00492A.

(8) Peng, X.; Satjaritanun, P.; Taie, Z.; Wiles, L.; Keane, A.; Capuano, C.; Zenyuk, I. V.; Danilovic, N. Insights into Interfacial and Bulk Transport Phenomena Affecting Proton Exchange Membrane Water Electrolyzer Performance at Ultra-Low Iridium Loadings. *Advanced Science* **2021**, *8* (21), 2102950. DOI: https://doi.org/10.1002/advs.202102950 (acccessed 2026/04/03).

(9) Sun, Z.; Wang, S.; Hu, X. Polymer-Functionalized Nanocatalysts: Engineering Interfaces and Microenvironments for Enhanced Catalysis. In *Polymers*, 2026; Vol. 18, p 465.

(10) Takimoto, D.; Toma, S.; Suda, Y.; Shirokura, T.; Tokura, Y.; Fukuda, K.; Matsumoto, M.; Imai, H.; Sugimoto, W. Platinum nanosheets synthesized via topotactic reduction of single-layer platinum oxide nanosheets for electrocatalysis. *Nature Communications* **2023**, *14* (1), 19. DOI: 10.1038/s41467-022-35616-4.

(11) Ando, S.; Yamamoto, E.; Kobayashi, M.; Osada, M. Atomic Layer Engineering of Pd Nanosheets for an Enhanced Hydrogen Evolution Reaction. *Nano Letters* **2024**, *24* (36), 11239-11245. DOI: 10.1021/acs.nanolett.4c02741.

(12) Ye, Z.; Chen, C.; Su, Y.; Feng, J.; Yin, Y. Templating Methods for Materials Fabrication Across Scales. *Chemical Reviews* **2026**, *126* (2), 717-798. DOI: 10.1021/acs.chemrev.5c00709.

(13) Kc, B. R.; Yusa, S.-i.; Bastakoti, B. P. Facile One-Pot Block Copolymer-Mediated Solvothermal Approach for Synthesis of High-Entropy Alloy with Enhanced OER Activity. *Precision Chemistry* **2026**, *4* (2), 165-172. DOI: 10.1021/prechem.5c00094.

(14) Jiang, B.; Guo, Y.; Kim, J.; Whitten, A. E.; Wood, K.; Kani, K.; Rowan, A. E.; Henzie, J.; Yamauchi, Y. Mesoporous Metallic Iridium Nanosheets. *Journal of the American Chemical Society* **2018**, *140* (39), 12434-12441. DOI: 10.1021/jacs.8b05206.

(15) Balasubramanian, R.; Kalaitzis, Z. M.; Cao, W. Solvent dependent morphologies in thiol-ene photopolymerization: A facile route to the synthesis of resorcinarene nanocapsules. *Journal of Materials Chemistry* **2010**, *20* (31), 6539-6543, 10.1039/C0JM00085J. DOI: 10.1039/C0JM00085J.
(16) Balasubramanian, R.; Prayakarao, S.; Han, S.; Cao, W. Tunable gold nanostructures with nanocapsules as template reaction vessels. *RSC Advances* **2012**, *2* (31), 11668-11671, 10.1039/C2RA21986G. DOI: 10.1039/C2RA21986G.